

This is the **accepted version** of the journal article:

Roth, Alison N.; Opare-Addo, Jemima; Gi, Eunbyeol; [et al.]. «Solution-phase synthesis and photoluminescence of quaternary chalcogenide semiconductors». *Chemistry of materials*, Vol. 35, Issue 5 (March 2023), p. 2165-2172. DOI 10.1021/acs.chemmater.3c00011

This version is available at <https://ddd.uab.cat/record/274565>

under the terms of the  **CC BY** license

Solution-Phase Synthesis and Photoluminescence of Quaternary Chalcohalide Semiconductors

Alison N. Roth,^{1,2} Jemima Opare-Addo,^{1,2} Eunbyeol Gi,^{1,2} Silvia Mena,³ Gonzalo Guirado,³ Richard D. Schaller,^{4,5} Emily A. Smith^{1,2} and Javier Vela^{*1,2}

¹US DOE Ames National Laboratory, Ames, Iowa 50011, United States; ²Department of Chemistry, Iowa State University, Ames, Iowa 50011, United States; ³Departament de Química, Universitat Autònoma de Barcelona, Bellaterra (Barcelona) 0819, Spain; ⁴Department of Chemistry, Northwestern University, Evanston, Illinois 60208, United States; ⁵Center for Nanoscale Materials, Argonne National Laboratory, Lemont, Illinois 60439, United States.

KEYWORDS. Chalcohalides, quaternary semiconductors, solution synthesis, photoluminescence.

ABSTRACT: Mixed-metal chalcohalide semiconductors have emerged as promising candidates for photovoltaic applications. However, preparation of these multinary compounds using solution-phase techniques remains particularly challenging compared to traditional solid-state methods. To fully harness their potential, it is desirable to develop synthetic methods that enable control over both the phase purity and dimensionality of chalcohalides. Here, we report the solution-phase synthesis of $\text{Pb}_2\text{SbS}_2\text{I}_3$ and $\text{Pb}_2\text{BiS}_2\text{I}_3$ quaternary chalcohalides using readily available precursors. Fine tuning of reaction parameters allows for the isolation of rod-like morphologies with tunable diameters and aspect ratios. Remarkably, these quaternary chalcohalides display photoluminescence as an ensemble as well as at the single particle level, as demonstrated using fluorescence microscopy. We further evaluate the relative stability and band gap of $\text{Pb}_2\text{SbS}_2\text{I}_3$ polymorphs and their coloring patterns using electronic structure calculations. The synthetic methods developed here will motivate the study of ever more complex chalcohalides and other multinary semiconductors for new technological applications.

Introduction

Chalcohalides are a special class of inorganic materials that have emerged as promising semiconductors for energy conversion devices.¹ Whereas chalcogenide semiconductors display high absorption coefficients and tunable band gaps but limited efficiency in solar devices,^{2,3,4} halide perovskites display higher power conversion efficiencies but lower chemical and thermal stability due to their weak ionic interactions.^{5,6,7} Occupying a promising middle between these two scenarios, mixed-ion chalcohalides are expected to combine the power conversion efficiency of halide perovskites with the enhanced stability of chalcogenides.^{8,9} Indeed, previous experimental and computational investigations have demonstrated the semiconducting nature of $\text{IV}_2\text{VS}_2\text{I}_3$ (IV = Sn, Pb; V = Sb, Bi) materials, with direct band gaps ranging from ~ 1.2 – 2.0 eV.^{10,11,12} Because these values are near the band gap that is ideal for photovoltaics, the first solar devices with $\text{Pb}_2\text{SbS}_2\text{I}_3$ ¹⁰ and $\text{Sn}_2\text{SbS}_2\text{I}_3$ ¹³ were fabricated, revealing promising power conversion efficiencies (PCE) of ~ 3 – 4% . The wider band gap compositions such as $\text{Pb}_2\text{SbS}_2\text{I}_3$ may also be of use in photocatalysis.⁸

$\text{IV}_2\text{VS}_2\text{I}_3$ chalcohalides are known to adopt either orthorhombic or monoclinic crystal structures (Figure 1).^{14,15} For example, $\text{Pb}_2\text{SbS}_2\text{I}_3$ can adopt a highly “disordered” orthorhombic (*Cmcm*) phase where one Pb atom occupies two

different positions at one site (positional disorder), and another crystallographic site can be occupied by either Pb or Sb (substitutional disorder). These types of disorder in $\text{Pb}_2\text{SbS}_2\text{I}_3$ are resolved at low temperature, resulting in a monoclinic (*P2₁/c*) structure.¹⁵ It remains unclear how the crystallographic disorder—or lack thereof—in $\text{Pb}_2\text{SbS}_2\text{I}_3$ affects the electronic properties for its two polymorphs.

The most common route used to synthesize $\text{IV}_2\text{VS}_2\text{I}_3$ chalcohalides involves solid-state reaction between the direct elements or between binary sulfides and iodides at relatively high (>500 °C) temperatures, which generally results in bulk material.^{11,15,16,17} Recently, an alternative route based on annealing films of $\text{Sn}_2\text{SbS}_2\text{I}_3$ that were solution-deposited from SbCl_3 , SnI_2 , and thiourea in DMF was successfully introduced.¹³ Similar success was achieved in the solution-phase synthesis of ternary semiconductors within the chalcohalide family: *Ternary* lead chalcohalides such as $\text{Pb}_4\text{S}_3\text{I}_2$ and $\text{Pb}_4\text{S}_3\text{Br}_2$ were prepared through solution-phase methods at relatively low (<200 °C) temperatures using metal halide and thiocyanate precursors.^{18,19} Similarly, BiSI nanorods were synthesized with control over particle size and morphology.²⁰ These findings strongly suggest that thiocyanate precursors, in combination with suitable coordinating organic ligands, may enable the synthetic development of more complex—and higher order—quaternary semiconductors.

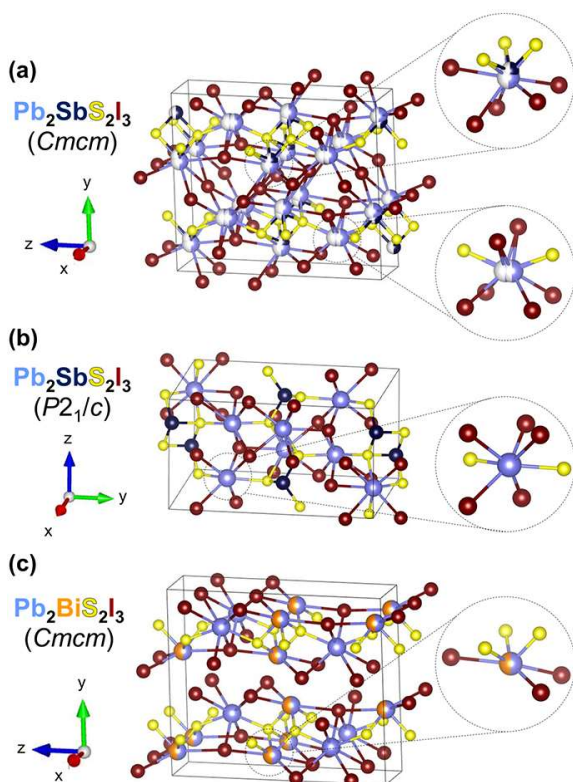


Figure 1. Unit cells of (a) orthorhombic ($Cmcm$) and (b) monoclinic ($P2_1/c$) $\text{Pb}_2\text{SbS}_2\text{I}_3$, and (c) orthorhombic ($Cmcm$) $\text{Pb}_2\text{BiS}_2\text{I}_3$. ($Cmcm$ $\text{Pb}_2\text{SbS}_2\text{I}_3$ exhibits both positional and substitutional disorder, while $\text{Pb}_2\text{BiS}_2\text{I}_3$ only exhibits substitutional disorder.)

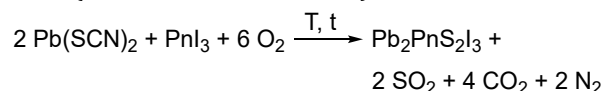
Here, we report the solution-phase synthesis of two such mixed-metal *quaternary* chalcogenides, $\text{Pb}_2\text{SbS}_2\text{I}_3$ and $\text{Pb}_2\text{BiS}_2\text{I}_3$, using commercially available thiocyanate and halide precursors. These chalcogenides exhibit highly anisotropic growth, giving rise to rod-like particles with aspect ratios that can be fine-tuned by changing the reaction conditions. We examine their ensemble as well as their single particle photoluminescence using a combination of spectroscopic techniques. Lastly, we compare our experimental results to new electronic structure calculations to better understand the effects of crystallographic disorder and polymorphism on the band gap of these materials.

Results and Discussion

Solution-Phase Synthesis and Structural Characterization. We first prepared $\text{Pb}_2\text{SbS}_2\text{I}_3$ and $\text{Pb}_2\text{BiS}_2\text{I}_3$ using a heat-up solution-phase synthesis approach starting from $\text{Pb}(\text{SCN})_2$, PbI_2 , and either SbI_3 or BiI_3 (Scheme 1, see Methods). X-ray diffraction (XRD) confirms that $\text{Pb}_2\text{SbS}_2\text{I}_3$ begins to form at temperatures as low as 180 °C. The reaction mixture goes

from a dark red solution at 160 °C to a bright orange solution between 180–270 °C. Formation of $\text{Pb}_2\text{BiS}_2\text{I}_3$ also occurs with a noticeable color change from light brown at 160 °C to a dark purple solution between 200–300 °C. However, unlike $\text{Pb}_2\text{SbS}_2\text{I}_3$, XRD indicates that phase-pure $\text{Pb}_2\text{BiS}_2\text{I}_3$ does not form until 300 °C, as evidenced by the presence of PbI_2 impurity peaks in the diffraction pattern below 280 °C.

Scheme 1. Solution-phase synthesis of quaternary chalcogenides ($\text{Pn} = \text{Sb}$ or Bi ; see Methods).^{21,22}



Inspection of the XRD patterns of the quaternary chalcogenides show that individual peaks are selectively attenuated—indicating preferred orientation—and/or broadened—indicating some small single crystalline domains (Figure 2, “heat-up”). For example, the (200) and (020) reflections are some of the weakest and broadest XRD reflections observed in solution-grown $\text{Pb}_2\text{SbS}_2\text{I}_3$ and $\text{Pb}_2\text{BiS}_2\text{I}_3$, which implies they correspond to short (less crystalline) stacking directions—along x(a) and y(b), respectively (see Supporting Information or SI). In contrast, the (004) reflection is the most intense and narrow XRD reflection observed in $\text{Pb}_2\text{BiS}_2\text{I}_3$, which implies it correspond to a long (more crystalline) stacking direction—along y(c). Indeed, scanning and transmission electron microscopy (SEM and TEM) reveal the two quaternary chalcogenides are highly anisotropic and crystalline (Figure 2), consistent with early reports of rod-like macroscopic or “bulk” crystals of $\text{Pb}_2\text{SbS}_2\text{I}_3$.^{11,15} High-resolution TEM (HR TEM) clearly shows that (040) planes are stacked across the smaller, diameter dimension of the rods, in agreement with these materials having anisotropic growth along the [001] direction.

The defining feature of the quaternary chalcogenide rods is their large length-to-diameter (l/w) aspect ratio, with $\text{Pb}_2\text{SbS}_2\text{I}_3$ exhibiting average width and length of 42 ± 14 nm and 1.7 ± 0.2 μm , respectively ($l/w = 40$) (Figure 2 and Table 1). Similarly, $\text{Pb}_2\text{BiS}_2\text{I}_3$ rods show average width and length of 630 ± 190 nm and 8.9 ± 2.1 μm , respectively ($l/w = 14$). The average $\text{Pb}_2\text{SbS}_2\text{I}_3$ rod width observed from SEM is consistent with the average single crystalline domain (Scherrer) size estimated from XRD peak widths (46 ± 28 nm). Energy dispersive X-ray spectroscopy (EDS) confirms the stoichiometry of each quaternary sample closely matches the theoretical composition of the desired $\text{IV}_2\text{VS}_2\text{I}_3$ phases although, in a few of our initial experiments, EDS revealed the presence of small amounts of an amorphous PbI_2 impurity (see SI and further optimization below).

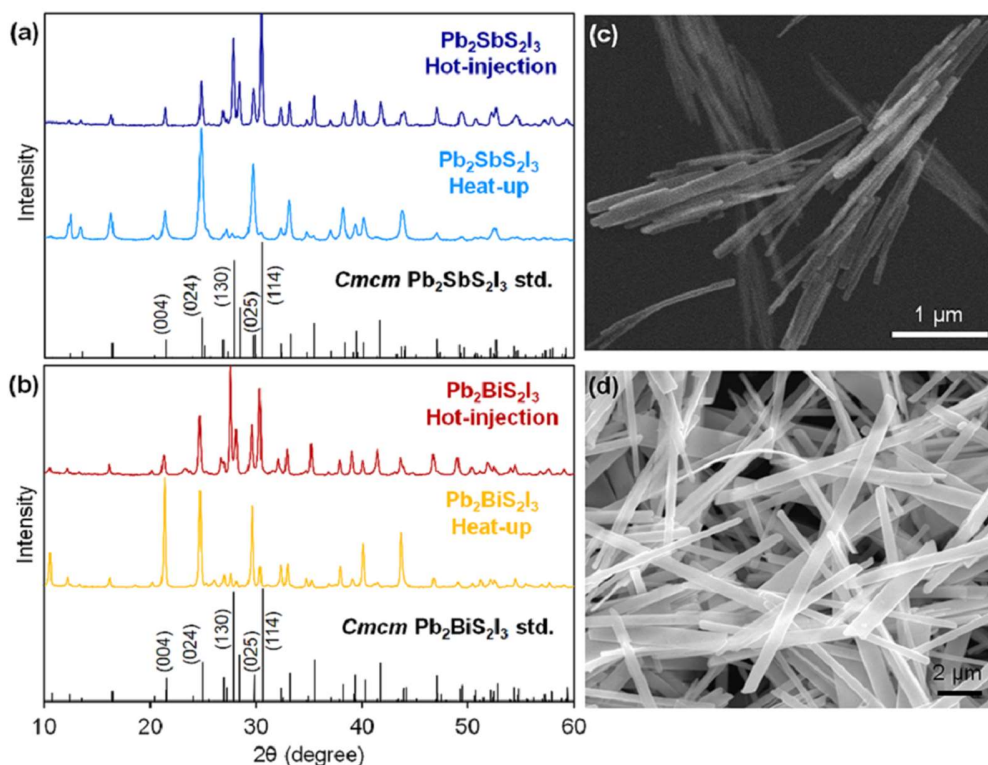


Figure 2. Solution-grown quaternary chalcogenides: (a, b) Powder XRD patterns of $\text{Pb}_2\text{SbS}_2\text{I}_3$ and $\text{Pb}_2\text{BiS}_2\text{I}_3$. SEM images of (c) $\text{Pb}_2\text{SbS}_2\text{I}_3$ and (d) $\text{Pb}_2\text{BiS}_2\text{I}_3$ rods prepared using the heat-up approach.

Further exploration of the best synthetic conditions showed that the exact ligand concentration has a significant impact on the formation of phase-pure quaternary chalcogenides. Specifically, higher concentrations of oleylamine lead to the formation of rock salt PbS . In some cases, increasing the concentration of both oleylamine and oleic acid results in a mixture of semicrystalline quaternary and ternary products. Similarly, increasing only the concentration of oleic acid leads to the formation of ternary $\text{Pb}_5\text{S}_2\text{I}_6$. The best results are obtained with relatively small concentrations of oleic acid and oleylamine (both at 76 mM) in octadecene, leading to the desired quaternary phases in phase pure form and, in the case of $\text{Pb}_2\text{SbS}_2\text{I}_3$, the smallest rod diameters (Table 1).

In addition to these findings, we learned that we can synthesize quaternary lead chalcogenides at slightly lower reaction temperatures without oleylamine. This is significant because oleylamine is highly corrosive and requires careful handling (see Methods). Furthermore, we can entirely omit PbI_2 as a precursor and instead hot-inject an oleic acid slurry of $\text{Pb}(\text{SCN})_2$ at 200 °C, which completely suppresses the formation of binary or ternary impurities. Using this hot-injection approach, we obtain $\text{Pb}_2\text{SbS}_2\text{I}_3$ and $\text{Pb}_2\text{BiS}_2\text{I}_3$ powder diffraction patterns that closely match the relative intensities in the orthorhombic standard patterns (Figure 2, “hot-injection”). Electron microscopy imaging still reveals distinct rod-like morphologies, although

both $\text{Pb}_2\text{SbS}_2\text{I}_3$ and $\text{Pb}_2\text{BiS}_2\text{I}_3$ have noticeably lower aspect ratios ($l/w = 8\text{--}9$) as compared to when they are made using the heat-up approach (Table 1).

Ensemble and Single Particle Optical Behavior. $\text{Pb}_2\text{SbS}_2\text{I}_3$ and $\text{Pb}_2\text{BiS}_2\text{I}_3$ are believed to be direct band gap semiconductors.^{11,13} Utilizing Tauc plots of the diffuse reflectance spectra (see Methods and SI), the band gap of $\text{Pb}_2\text{SbS}_2\text{I}_3$ is extrapolated to be *ca.* 1.9 eV which agrees with its bright orange color. $\text{Pb}_2\text{BiS}_2\text{I}_3$ exhibits a slightly narrower band gap of 1.6 eV, consistent with its dark purple color (Figure 3). Interestingly, chalcogenides prepared using the hot-injection approach exhibit slightly red-shifted absorption onsets compared to those made using the heat-up approach. In the case of $\text{Pb}_2\text{SbS}_2\text{I}_3$, this could arise from their smaller diameter and thus to a degree of quantum confinement. The band gaps of these materials roughly parallel those obtained using a combination of X-ray photoelectron spectroscopy (XPS)^{23,24} and cyclic voltammetry (CV)^{25,26,27,28,29} (see SI).

Upon excitation at 450 nm, crude solutions of $\text{Pb}_2\text{SbS}_2\text{I}_3$ emit at ~ 650 nm (1.91 eV) (Figure 3). Consecutive washes considerably decrease the overall PL intensity. Time-correlated single photon counting (TCSPC) shows that the $\text{Pb}_2\text{SbS}_2\text{I}_3$ rods have an average, ensemble PL lifetime of 1.2 ns and a quantum yield (QY) <1%.

□

Table 1. Representative properties of solution-grown quaternary chalcogenide semiconductors.

Pb prec(s.) (mmol) ^a	Pnictide prec. (mmol) ^b	Ligands ^c (mL)	T (°C)	t (min)	Product	App. gap (eV) ^d	Width ^e (Scherrer) ^f (nm)	Length ^e (μm)	Aspect ratio (l/w)
Pb(SCN) ₂ (0.2), PbI ₂ (0.1)	SbI ₃ (0.1)	Oleic acid (0.25), oleylNH ₂ (0.25)	270	1	Pb ₂ SbS ₂ I ₃ (<i>Cmcm</i>)	1.9	42±14 (46±28)	1.7±0.2	40
Pb(SCN) ₂ (0.2)	SbI ₃ (0.1)	Oleic acid (8)	250	1	Pb ₂ SbS ₂ I ₃ (<i>Cmcm</i>)	1.6	400±120 (380±120)	3.2±0.9	8
Pb(SCN) ₂ (0.2), PbI ₂ (0.1)	BiI ₃ (0.1)	Oleic acid (0.25), oleylNH ₂ (0.25)	300	1	Pb ₂ BiS ₂ I ₃ (<i>Cmcm</i>)	1.6	630±190 (427±464)	8.9±2.1	14
Pb(SCN) ₂ (0.2), PbI ₂ (0.1)	BiI ₃ (0.1)	Oleic acid (8)	250	1	Pb ₂ BiS ₂ I ₃ (<i>Cmcm</i>)	1.3	240±60 (260±190)	2.3±0.4	10

^a[Pb]_T = 19–29 mM. ^b[Pn]_T = 9.5 mM. ^cODE volume = 10.5 mL (V_T) - oleic acid volume - oleylNH₂ volume. ^dEstimated using Tauc plots (see Methods). ^eFrom EM. ^fFrom XRD.

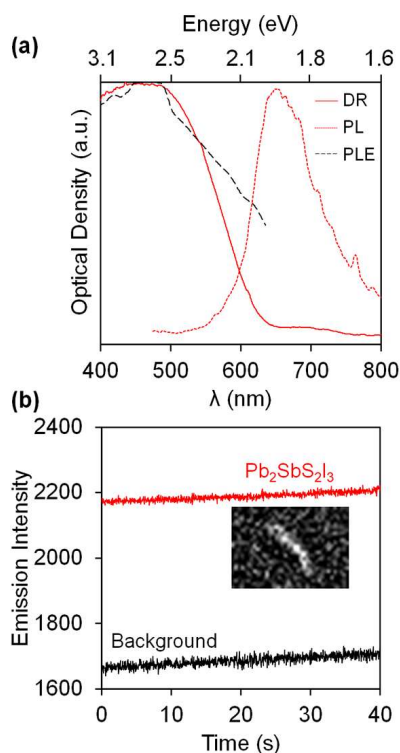


Figure 3. (a) Diffuse reflectance (DR, solid red line), photoluminescence (PL, red-dashed line), and photoluminescence excitation (PLE, red-dashed line, $\lambda_{em} = 650$ nm) spectra of solid film of Pb₂SbS₂I₃ nanorods (b) Photoluminescence of a single Pb₂SbS₂I₃ rod over time ($\lambda_{exc} = 450$ nm, with a 629±56 nm emission filter). (Movies available in the Supporting Information).

Interestingly, Pb₂SbS₂I₃ rods are photoluminescent even at the single particle level. Unlike the blinking behavior that is ubiquitous in colloidal CdSe and other nanocrystal quantum dots and nanowires,³⁰ fluorescence microscopy reveals that individual Pb₂SbS₂I₃ rods display steady, shape-correlated photoluminescence over time, with no OFF periods or blinking recorded under continuous photoexcitation at 450 nm (Figure 3 and SI movie). Moreover, rather than fading or staying constant, the rods' emission intensity appears to gradually increase over time. Interestingly, this lack of fluorescence intermittency is similar

to what has been reported for lead halide perovskites.³¹ Lead-halide interactions are often defect tolerant due to the presence of Pb²⁺ 6s² lone pair bonding contributions.^{32,33} This unique electronic structure results in shallow defect states in the band gap or within the valence band which can ultimately improve and increase photoluminescence stability.³⁴ Moreover, similar to binary nanocrystals (CdSe, etc.), reduction and even complete suppression of blinking in lead halide perovskites has also been achieved by surface passivation, either with ligands³⁵ or by growing protective shells over the core material.³⁶ These modifications lead to the elimination of nonradiative Auger recombination arising from structural defects and charge carrier trap states.^{37,38} Therefore, our findings bode well for the use of quaternary chalcogenide semiconductor nanoparticles in a wide range of optoelectronic applications and devices.

Polymorphism and Coloring from Electronic Structure Calculations. To better understand the polymorphism and optoelectronic properties of the quaternary chalcogenides, we turned to relative energy calculations using the Vienna *Ab initio* Simulation Package (VASP).³⁹ Because the reported orthorhombic *Cmcm* structure exhibits mixed Pb/Sb occupancy sites, we modeled various supercell structures with different arrangements of Pb and Sb at those positions (see Methods).^{40,41} The different possible “coloring” patterns for the *Cmcm* Pb₂SbS₂I₃ supercell can be described by the orientation of Pb and Sb atoms stacked along the [010] direction: Specifically, Pb and Sb sites can alternate completely (*staggered*); the same types of atoms can face each other (*Pb-Pb/Sb-Sb facing*); or the opposite types of atoms can face each other (*Alt. Pb-Sb facing*) (Figure 4). After fully relaxing the unit cells, the *Pb-Sb facing* and (*Alt.*) *Pb-Sb facing* supercells maintained orthorhombic structures (*Pca2*₁ and *Pna2*₁, respectively). In contrast, the *Pb-Pb/Sb-Sb facing* and *staggered* supercells relaxed into monoclinic structures (*P2* and *P2*₁/*c*, respectively). Out of the four different coloring patterns modeled, the *staggered* supercell structure has the lowest total energy, closely resembling the relative energy and atomic coloring pattern of the *P2*₁/*c* polymorph (see SI).

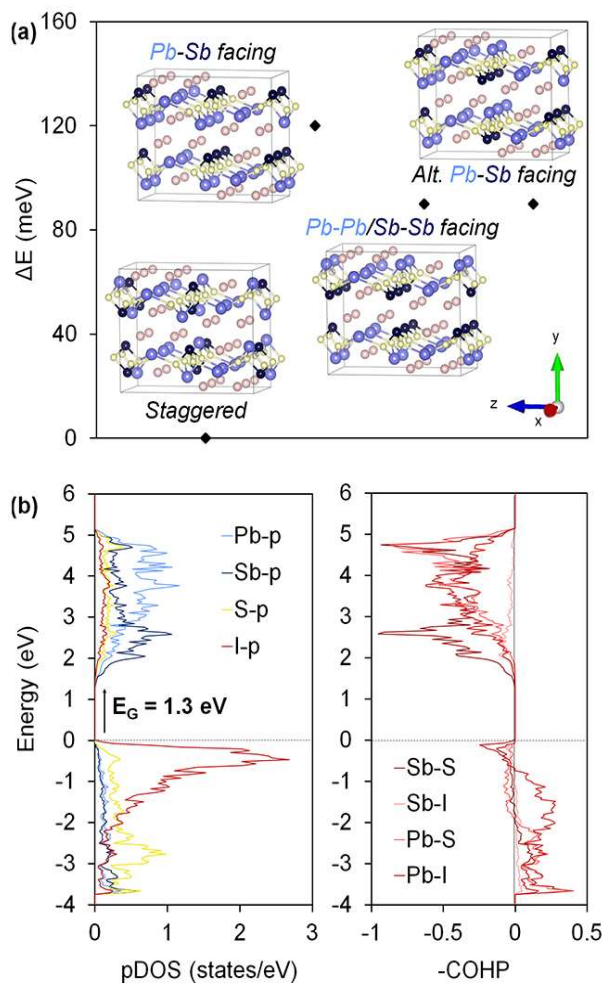


Figure 4. (a) Relative energies of different *Cmcm* $\text{Pb}_2\text{SbS}_2\text{I}_3$ supercell structures (Note: for clarity, some *Pb/Sb-S/I* bonds are omitted and the *S* and *I* atoms are faded). (b) Partial density of states (pDOS) (left) and COHP (right) of the *staggered* supercell structure of $\text{Pb}_2\text{SbS}_2\text{I}_3$.

Density of states (DOS) calculations provide further insight into the more likely coloring pattern of the disordered $\text{Pb}_2\text{SbS}_2\text{I}_3$ polymorph. Using the tight-binding linear muffin-tin orbital atomic sphere approximation (TB-LMTO-ASA) method,⁴² we calculated the DOS of each of the different supercells and determined their band gap values (SI). The DOS of the lowest energy *staggered* polymorph shows a band gap of 1.30 eV (Figure 4), which underestimates the experimentally determined gap (1.9 eV) by *ca.* 30%. The remaining supercells display much narrower band gaps, which underestimate the experimental value by 50–75%. Considering both the degree of band gap underestimation often observed using TB-LMTO,^{43,44,45} as well as the relative total energies, these findings suggest that the *Cmcm* $\text{Pb}_2\text{SbS}_2\text{I}_3$ polymorph most likely adopts the *staggered* coloring pattern. Because different *Pb/Sb* coloring patterns appear to affect the calculated band gap, it may be possible to achieve band gap tunability by controlling the extent of crystallographic disorder in $\text{Pb}_2\text{SbS}_2\text{I}_3$.

Analysis of the DOS of the *P2₁/c* $\text{Pb}_2\text{SbS}_2\text{I}_3$ polymorph shows a nearly identical band gap (1.35 eV) and pDOS

features compared to the *staggered* polymorph. For both of the lowest energy $\text{Pb}_2\text{SbS}_2\text{I}_3$ polymorphs, the valence band region of the DOS is dominated primarily by *I-p* and *S-p* orbitals, while *Pb-p* and *Sb-p* orbitals significantly contribute to the conduction band region. These features are consistent with the DOS features of *Pb* and *Sn*-based quaternary bismuth chalcogenides,¹¹ as well as with our own control calculation for $\text{Pb}_2\text{BiS}_2\text{I}_3$. A comparison of the Crystal Orbital Hamilton Population (COHP)⁴⁶ for the two $\text{Pb}_2\text{SbS}_2\text{I}_3$ polymorphs, however, shows a higher degree of filled *Pb-I* antibonding states below the Fermi level for the *P2₁/c* phase, as reflected in the negative portion of the COHP diagram (see SI). This may suggest that formation of the disordered phase is more favorable overall, despite both $\text{Pb}_2\text{SbS}_2\text{I}_3$ polymorphs being very close in energy. Considering that the completely ordered *P2₁/c* phase has only been isolated at low temperatures (100 K),¹⁵ it is plausible that the disordered (*Cmcm*) polymorph that we observe experimentally is metastable. In this case, our calculations agree well with experiment and offer physical insight into the effects of coloring and polymorphism in $\text{Pb}_2\text{SbS}_2\text{I}_3$ and similar quaternary chalcogenides.

Conclusions

In summary, we have successfully developed the solution-phase synthesis of quaternary mixed-metal chalcogenides using both heat-up and hot-injection approaches in combination with commercially available halide and thiocyanate precursors. We demonstrate control over the diameter and aspect ratio of their highly anisotropic, rod-like particles by adjusting ligand concentration, resulting in widths as small as *ca.* 40 nm. Both $\text{Pb}_2\text{SbS}_2\text{I}_3$ and $\text{Pb}_2\text{BiS}_2\text{I}_3$ rods exhibit direct band gap values below 2.0 eV, and $\text{Pb}_2\text{SbS}_2\text{I}_3$ shows photoluminescence behavior both in solution and at the single particle level. Electronic structure calculations reveal that the disordered $\text{Pb}_2\text{SbS}_2\text{I}_3$ phase likely adopts a *staggered* atomic coloring pattern and, consequently, has nearly identical electronic and structural features to the *P2₁/c* polymorph.

Many additional compositional variations are possible within this family of mixed-metal chalcogenides, including those that contain different chalcogens (Se, Te), halogens (Cl, Br), and chalcogen-to-halogen ratios. Because there is a heightened demand to develop semiconductors that are lead-free, tin-based analogs such as $\text{Sn}_2\text{BiS}_2\text{I}_3$ and $\text{Sn}_2\text{SbS}_2\text{I}_3$ will be particularly attractive alternatives but their solution-phase synthesis has yet to be thoroughly explored.¹² The methods developed in this study are a stepping stone toward synthesizing such quaternary materials. Further preparative and computational investigations of these materials will be needed to move them closer to real-life application and deployment.

Methods

Materials. Oleylamine (oleylNH₂, technical grade, 70%), 1-octadecene (ODE, technical grade, 90%), lead(II) thiocyanate ($\text{Pb}(\text{SCN})_2$, 99.5%), and lead(II) iodide (PbI_2 , 99%) were purchased from Sigma Aldrich; antimony(III) iodide (SbI_3 , 99.9%) and bismuth(III) iodide (BiI_3 , 99.999%) from Strem; oleic acid (OA, technical grade, 90%) from Alfa Aesar; hexanes (99.9%) and methanol (99.9%) from

□

Fisher. All chemicals were used as received. *Caution: Oleylamine is a highly corrosive liquid and must be handled with extreme care and in the smallest amounts possible.*

Synthesis. All reactions were carried out under air. *Heat-up Method.* $\text{Pb}(\text{SCN})_2$ (0.2 mmol), PbI_2 (0.1 mmol) and either SbI_3 or BiI_3 (0.1 mmol) were stirred together in a 100 mL round bottom flask containing 1-octadecene (10 mL, 31 mmol), oleic acid (0.25 mL, 0.8 mmol) and oleylamine (0.25 mL, 0.8 mmol) at 110 °C until all solids dissolved. The solution was heated to 270 °C ($\text{Pb}_2\text{SbS}_2\text{I}_3$) or 300 °C ($\text{Pb}_2\text{BiS}_2\text{I}_3$) for 1 min and subsequently cooled to room temperature (R.T.). *Hot-injection Method.* Alternatively, quaternary lead chalcogenides are prepared by injecting a slurry of $\text{Pb}(\text{SCN})_2$ (0.2 mmol) in oleic acid (2 mL, 6.3 mmol) into a solution of SbI_3 or BiI_3 (0.1 mmol) in oleic acid (6 mL, 19 mmol) and 1-octadecene (2.5 mL, 7.8 mmol) at 200 °C, followed by heating the mixture to 250 °C for 1 min before cooling to R.T. *Purification.* Crude chalcogenide solutions were initially centrifuged at 4500 rpm for 5 min followed by discarding the supernatant. The pellet was then resuspended in hexanes and methanol (5 mL of each) and centrifuged again to remove excess ligands.

Structural Characterization. Powder X-ray diffraction (XRD) was measured on a Rigaku Ultima IV diffractometer (40 kV, 44 mA) using $\text{Cu K}\alpha$ radiation on a zero-background quartz sample holder. Transmission electron microscopy (TEM) imaging was performed on a JEOL 2100 scanning transmission electron microscope. Samples were prepared by drop casting dilute solution in hexanes onto a carbon-coated 200 mesh copper grid. Scanning electron microscopy (SEM) images were acquired on a JEOL JSM-IT200 scanning electron microscope.

Optical Characterization. Diffuse-reflectance spectra were collected using a SL1 Tungsten Halogen lamp (vis-IR), a SL3 Deuterium Lamp (UV), and a BLACK-Comet C-SR-100 spectrometer (200–1080 nm). The band gap values were estimated by extrapolating the linear slope of Tauc plots by plotting $(\text{Ahv})^r$ versus $h\nu$ (A = absorbance, $h\nu$ = incident photon energy in eV, $r = 1/2$ for direct semiconductors).⁴⁷ Photoluminescence (PL) spectra were collected on a Horiba Jobin Yvon Fluorolog-3 spectrofluorometer (Slit width = 5 nm; $\lambda_{\text{exc}} = 450$ nm). The crude samples were suspended in hexanes for the solution-phase photoluminescence measurements. Photoluminescence excitation (PLE) spectra of $\text{Pb}_2\text{SbS}_2\text{I}_3$ were collected by monitoring photoluminescence (PL) emission at 650 nm while varying the excitation wavelength between 250–635 nm. TSCPC was performed using a 405 nm Picoquant laser operating at 2.5 MHz and 50 ps pulsewidth. Photons produced by the sample were directed into a 0.3 m spectrograph with a CCD for spectral measurement or avalanche photodiode for dynamics. Each selected emission wavelength was collected for 600 s.

Single Particle Fluorescence Microscopy. Single particle photoluminescence (PL) was recorded on an inverted microscope operated in epifluorescence mode (Nikon Eclipse TE2000U Melville, NY) fitted with a 100x (1.49 NA) oil immersion objective. An Xcite Series 120 PC mercury lamp with a 450±50 nm excitation filter and a

629±56 nm emission filter were used. $\text{Pb}_2\text{SbS}_2\text{I}_3$ nanocrystals were diluted in hexanes and sonicated for 90 min before depositing 50 μL on a glass microscope coverslip (Fisher Scientific, Pittsburgh, PA). The solvent was removed under vacuum and the sample was dried after 15 min. Single particle PL movies were collected on an Andor iXon Ultra EMCCD camera (Oxford Instruments, Abingdon, UK) with 40 ms exposure time and 70x EM gain. Each movie was 40 s in duration and 5 movies were collected. ImageJ was used to analyze the PL intensity versus time for the selected particles and background.

Cyclic Voltammetry. Electrochemical studies were performed by cyclic voltammetry (CV) using the potentiostat Workstation CHInstrument and controlled by the software CHI660e V14.08. A three-electrode system and a thermostatic electrochemical cell was used. Glassy carbon (WEc, 3 mm of diameter) was used as working electrode, while a platinum wire and a saturated calomel electrode (SCE) were used as counter (CE), and reference (RE) electrodes, respectively. Both CE and RE electrodes were separated from the solution by a salt-bridge. The working electrode was carefully polished with 1 mm diamond paste (DP-Paste, P) and rinsed with ethanol. Dispersion solutions from 0.5 to 1 mg/mL of each chalcogenide semiconductor was prepared in hexanes and sonicated for 1–2 minutes. Once the dispersions were prepared, 50 μL of each sample was drop-cast onto the glassy carbon electrode surface ($d = 3$ mm). After the hexanes fully evaporated, CV at different scan rates ($v = 0.05$ to 0.5 V s^{-1}) was performed using the chalcogenide modified electrode (working electrode, WE) in a pure acetonitrile + 0.1 M of tetrabutylammonium tetrafluoroborate (TBABF_4) solution under a nitrogen atmosphere. Prior to recording the cyclic voltammograms, blank experiments were performed to ensure that the glassy carbon surface of the WE was well polished, fresh and clean. Hence, no electrochemical signals were detected for non-modified working electrodes in the selected potential range (-2.5–1.5 V).

X-ray photoelectron spectroscopy. XPS measurements were collected with a Kratos Amicus/ESCA 3400 instrument. The powder chalcogenide samples were first pressed into 8 mm (diameter) by 1.2 mm (height) pellets with a cold pellet press. The pellets were irradiated with 240 W un-monochromated $\text{Mg K}\alpha$ X-rays, and photoelectrons emitted at 0° from the surface were energy analyzed using a DuPont type analyzer. The pass energy was set at 150 eV. The binding energy of C 1s at 284.6 eV was used for reference.

Calculations. Relative energy calculations were performed using the Vienna Ab initio Simulation Package (VASP),^{39,48} with projected augmented-wave (PAW) pseudopotentials.⁴⁹ Electronic exchange-correlation was treated using the Perdew-Burke-Ernzerhof (PBE) functional.⁵⁰ The cut-off energy for the plane wave basis functions was 500 eV. During the structural optimizations the volume, atomic positions and cell shape were allowed to relax until the convergence energy was less than 1×10^{-4} eV. The relative total energies were calculated using the tetrahedron method over a $16 \times 16 \times 16$ k-point grid. Unit

□

cell representations were generated using VESTA.⁵¹ To deal with the disordered Pb/Sb or Pb/Bi sites, supercell structures of *Cmcm* Pb₂SbS₂I₃ and *Cmcm* Pb₂BiS₂I₃ were constructed by doubling the *a*-lattice parameter and coloring the unit cell to assign a single atom to the mixed occupation sites. Density of states (DOS) and Crystal orbital Hamilton populations (COHP)⁴⁶ were calculated using the tight binding linear muffin-tin orbital atomic sphere approximation (TB-LMTO-ASA) package.⁴² The DOS and COHPs were calculated using the tetrahedron method after converging the total energy on a k-mesh of 7×6×12 (*Cmcm* Pb₂SbS₂I₃ and *Cmcm* Pb₂BiS₂I₃) or 14×6×12 (*P2₁/c* Pb₂SbS₂I₃) in the irreducible wedge of the Brillouin zone.

ASSOCIATED CONTENT

Supporting Information. SEM, TEM, EDS, XRD, diffuse reflectance, PL, TCSPC, single-particle fluorescence microscopy movies, XPS, cyclic voltammograms, DOS and COHP calculations are provided in the supporting information. This material is available free of charge via the Internet at <http://pubs.acs.org>.

AUTHOR INFORMATION

Corresponding Author

Javier Vela – US DOE Ames National Laboratory, Ames, Iowa 50011, United States, and Department of Chemistry, Iowa State University, Ames, Iowa 50011, United States. Email: vela@iastate.edu

ACKNOWLEDGMENT

This work was supported by the Ames National Laboratory's Laboratory Directed Research and Development (LDRD) program. The Ames Laboratory is operated for the U.S. Department of Energy by Iowa State University under Contract DE-AC02-07CH11358. G.G. and S.M. thank the Ministerio de Ciencia e Innovación of Spain for financial support through project PID2019-106171RB-I00. S.M. acknowledges support from the Margarita Salas UCM postdoctoral grants funded by the Spanish Ministry of Universities with European Union funds - NextGenerationEU. Work performed at the Center for Nanoscale Materials, a U.S. Department of Energy Office of Science User Facility, was supported by the U.S. DOE, Office of Basic Energy Sciences, under Contract No. DE-AC02-06CH11357. We thank Dapeng Jing, Marquix Adamson, and Phil Yox for assistance with XPS, SEM, and COHP calculations, respectively.

REFERENCES

- ¹ Huang, Y. T.; Kavanagh, S. R.; Scanlon, D. O.; Walsh, A.; Hoyer, R. L. Z. Perovskite-Inspired Materials for Photovoltaics and Beyond—From Design to Devices. *Nanotechnology* **2021**, *32*, 132004-1–132004-60.
- ² Moon, M. M. A.; Rahman, M. F.; Kamruzzaman, M.; Hossain, J.; Ismail, I. B. M. Unveiling the Prospect of a Novel Chemical Route for Synthesizing Solution-Processed CdS/CdTe Thin-Film Solar Cells. *Energy Rep.* **2021**, *7*, 1742–1756.
- ³ Gu, M.; Wang, Y.; Yang, F.; Lu, K.; Xue, Y.; Wu, T.; Fang, H.; Zhou, S.; Zhang, Y.; Ling, X.; Xu, Y.; Li, F.; Yuan, J.; Loi, M. A.; Liu, Z.; Ma, W. Stable PbS Quantum Dot Ink for Efficient Solar Cells by Solution-Phase Ligand Engineering. *J. Mater. Chem. A* **2019**, *7*, 15951–15959.
- ⁴ Li, Z.; Liang, X.; Li, G.; Liu, H.; Zhang, H.; Guo, J.; Chen, J.; Shen, K.; San, X.; Yu, W. 9.2%-Efficient Core-Shell Structured Antimony Selenide Nanorod Array Solar Cells. *Nat. Commun.* **2019**, *10*, 125-1–125-9.
- ⁵ Akkerman, Q. A.; Nguyen, T. P. T.; Boehme, S. C.; Montanarella, F.; Dirin, D. N.; Wechsler, P.; Beiglböck, F.; Rainò, G.; Erni, R.; Katan, C.; Even, J.; Kovalenko, M. V. Controlling the Nucleation and Growth Kinetics of Lead Halide Perovskite Quantum Dots. *Science* **2022**, *377*, 1406–1412.
- ⁶ Sidhik, S.; Wang, Y.; De Siena, M.; Asadpour, R.; Torma, A. J.; Terlier, T.; Ho, K.; Li, W.; Puthirath, A. B.; Shuai, X.; Agrawal, A.; Traore, B.; Jones, M.; Giridharagopal, R.; Ajayan, P. M.; Strzalka, J.; Ginger, D. S.; Katan, C.; Alam, M. A.; Even, J.; Kanatzidis, M. G.; Mohite, A. D. Deterministic Fabrication of 3D/2D Perovskite Bilayer Stacks for Durable and Efficient Solar Cells. *Science* **2022**, *377*, 1425–1430.
- ⁷ Sakhatskyi, K.; John, R. A.; Guerrero, A.; Tsarev, S.; Sabisch, S.; Das, T.; Matt, G. J.; Yakunin, S.; Cherniukh, I.; Kotyrba, M.; Berezovska, Y.; Bodnarchuk, M. I.; Chakraborty, S.; Bisquert, J.; Kovalenko, M. V. Assessing the Drawbacks and Benefits of Ion Migration in Lead Halide Perovskites. *ACS Energy Lett.* **2022**, *7*, 3401–3414.
- ⁸ Ganose, A. M.; Savory, C. N.; Scanlon, D. O. Beyond Methylammonium Lead Iodide: Prospects for the Emergent Field of ns² Containing Solar Absorbers. *Chem. Commun.* **2017**, *53*, 20–44.
- ⁹ Xiao, J. R.; Yang, S. H.; Feng, F.; Xue, H. G.; Guo, S. P. A Review of the Structural Chemistry and Physical Properties of Metal Chalcogenide Halides. *Coord. Chem. Rev.* **2017**, *347*, 23–47.
- ¹⁰ Nie, R.; Kim, B.; Hong, S. T.; Seok, S. I. Nanostructured Heterojunction Solar Cells Based on Pb₂SbS₂I₃: Linking Lead Halide Perovskites and Metal Chalcogenides. *ACS Energy Lett.* **2018**, *3*, 2376–2382.

□

-
- ¹¹ Islam, S. M.; Malliakas, C. D.; Sarma, D.; Maloney, D. C.; Stoumpos, C. C.; Kontsevoi, O. Y.; Freeman A. J.; Kanatzidis, M. G. Direct Gap Semiconductors $\text{Pb}_2\text{BiS}_2\text{I}_3$, $\text{Sn}_2\text{BiS}_2\text{I}_3$, and Sn_2BiSI_5 . *Chem. Mater.* **2016**, *28*, 7332–7343.
- ¹² C. Yang, Z. Wang, G. He, H. Zhang and C. Liao, *ACS Appl. Nano Mater.*, 2022, **5**, 16033–16038.
- ¹³ Nie, R.; Lee, K. S.; Hu, M.; Paik, M. J.; Seok, S. I. Heteroleptic Tin-Antimony Sulfoiodide for Stable and Lead-Free Solar Cells. *Matter.* **2020**, *3*, 1701–1713.
- ¹⁴ Starosta, V. I.; Kroutil, J.; Benes, L. Preparation and Fundamental Physical Properties of $\text{Sn}_2\text{SbS}_2\text{I}_3$ and $\text{Pb}_2\text{SbS}_2\text{I}_3$ Compounds. *Cryst. Res. Technol.* **1990**, *25*, 1439–1442.
- ¹⁵ Doussier, C.; Moëlo, Y.; Léone, P.; Meerschaut, A.; Evain, M. Crystal Structure of $\text{Pb}_2\text{SbS}_2\text{I}_3$, and Re-Examination of the Crystal Chemistry within the Group of (Pb/Sn/Sb) Chalcogeno-Iodides. *Solid State Sci.* **2007**, *9*, 792–803.
- ¹⁶ Dolgikh, V. A. Preparation of Single Crystals and Dielectric Properties of $\text{Sn}_2\text{SbS}_2\text{I}_3$ and $\text{Pb}_2\text{SbS}_2\text{I}_3$. *Izv. Akad. Nauk SSSR Neorg. Mater.* **1985**, *21*, 1215–1218.
- ¹⁷ Ibanez, A.; Jumas, J. C.; Olivier-Fourcade, J.; Philippot, E. Synthesis and Characterization of Antimony and Tin Chalcogenoiodides. *Rev. Chim. Miner.* **1984**, *21*, 344–357.
- ¹⁸ Toso, S.; Akkerman, Q. A.; Martín-García, B.; Prato, M.; Zito, J.; Infante, I.; Dang, Z.; Moliterni, A.; Giannini, C.; Blatt, E.; Lobato, I.; Ramade, J.; Bals, S.; Buha, J.; Spirito, D.; Mugnaioli, E.; Gemmi, M.; Manna, L. Nanocrystals of Lead Chalcogenides: A Series of Kinetically Trapped Metastable Nanostructures. *J. Am. Chem. Soc.* **2020**, *142*, 10198–10211.
- ¹⁹ Imran, M.; Peng, L.; Pianetti, A.; Pinchetti, V.; Ramade, J.; Zito, J.; Di Stasio, F.; Buha, J.; Toso, S.; Song, J.; Infante, I.; Bals, S.; Brovelli, S.; Manna, L. Halide Perovskite–Lead Chalcogenide Nanocrystal Heterostructures. *J. Am. Chem. Soc.* **2021**, *143*, 1435–1446.
- ²⁰ Quarta, D.; Toso, S.; Giannuzzi, R.; Caliandro, R.; Moliterni, A.; Saleh, G.; Capodilupo, A. L.; Debellis, D.; Prato, M.; Nobile, C.; Maiorano, V.; Infante, I.; Gigli, G.; Giannini, C.; Manna, L.; Giansante, C. Colloidal Bismuth Chalcogenide Nanocrystals. *Angew. Chem. Int. Ed.* **2022**, *134*, e202201747-1–e202201747-8.
- ²¹ Akkerman, Q. A.; Martín-García, B.; Buha, J.; Almeida, G.; Toso, S.; Marras, S.; Bonaccorso, F.; Petralanda, U.; Infante, I.; Manna, L. Ultrathin Orthorhombic PbS Nanosheets. *Chem. Mater.* **2019**, *31*, 8145–8153.
- ²² Ptaszyński, B.; Skiba, E.; Krystek, J. Thermal Decomposition of Bi(III), Cd(II), Pb(II) and Cu(II) Thiocyanates. *J. Therm. Anal. Calorim.* **2001**, *65*, 231–239.
- ²³ Kahn, A. Fermi Level, Work Function and Vacuum Level. *Mater. Horiz.* **2016**, *3*, 7–10.
- ²⁴ Whittles, T. J.; Veal, T. D.; Savory, C. N.; Welch, A. W.; Lucas, F. W.; Gibbon, J. T.; Birkett, M.; Potter, R. J.; Scanlon, D. O.; Zakutayev, A.; Dhanak, V. R. Core Levels, Band Alignments, and Valence-Band States in CuSbS_2 for Solar Cell Applications. *ACS Appl. Mater. Interfaces* **2017**, *9*, 41916–41926.
- ²⁵ Ravi, V. K.; Markad, G. B.; Nag, A. Band Edge Energies and Excitonic Transition Probabilities of Colloidal CsPbX_3 ($X = \text{Cl}, \text{Br}, \text{I}$) Perovskite Nanocrystals. *ACS Energy Lett.* **2016**, *1*, 665–671.
- ²⁶ Ingole, P. P.; Markad, G. B.; Saraf, D.; Tatikondewar, L.; Nene, O.; Kshirsagar, A.; Haram, S. K. Band Gap Bowing at Nanoscale: Investigation of $\text{CdS}_x\text{Se}_{1-x}$ Alloy Quantum Dots through Cyclic Voltammetry and Density Functional Theory. *J. Phys. Chem. C* **2013**, *117*, 7376–7383.
- ²⁷ Elgrishi, N.; Rountree, K. J.; McCarthy, B. D.; Rountree, E. S.; Eisenhart, T. T.; Dempsey, J. L. A Practical Beginner's Guide to Cyclic Voltammetry. *J. Chem. Educ.* **2018**, *95*, 197–206.
- ²⁸ Jadhav, Y. A.; Thakur, P. R.; Haram, S. K. Voltammetry Investigation on Copper Zinc Tin Sulphide /Selenide ($\text{CZTS}_x\text{Se}_{1-x}$) Alloy Nanocrystals: Estimation of Composition Dependent Band Edge Parameters. *Sol. Energy Mater. Sol. Cells* **2016**, *155*, 273–279.
- ²⁹ Sun, Z.; Ma, T.; Tao, H.; Fan, Q.; Han, B. Fundamentals and Challenges of Electrochemical CO_2 Reduction Using Two-Dimensional Materials. *Chem* **2017**, *3*, 560–587.
- ³⁰ Glennon, J. J.; Tang, R.; Buhro, W. E.; Loomis, R. A. Synchronous Photoluminescence Intermittency (Blinking) along Whole Semiconductor Quantum Wires. *Nano Lett.* **2007**, *7*, 3290–3295.
- ³¹ Zhu, F.; Men, L.; Guo, Y.; Zhu, Q.; Bhattacharjee, U.; Goodwin, P. M.; Petrich, J. W.; Smith, E. A.; Vela, J. Shape Evolution and Single Particle Luminescence of Organometal Halide Perovskite Nanocrystals. *ACS Nano* **2015**, *9*, 2948–2959.
- ³² Ye, J.; Byrnavand, M. M.; Martínez, C. O.; Hoyer, R. L. Z.; Saliba, M.; Polavarapu, L. Defect Passivation in Lead-Halide Perovskite Nanocrystals and Thin Films: Toward Efficient LEDs and Solar Cells. *Angew. Chem.* **2021**, *133*, 21804–21828.
- ³³ Brandt, R. E.; Stevanović, V.; Ginley, D. S.; Buonassisi, T. Identifying Defect-Tolerant Semiconductors with High Minority Carrier Lifetimes: Beyond Hybrid Lead Halide Perovskites. *MRS Commun.* **2015**, *5*, 265–275.
- ³⁴ Huang, H.; Bodnarchuk, M. I.; Kershaw, S. V.; Kovalenko, M. V.; Rogach, A. L. Lead Halide Perovskite Nanocrystals in the Research Spotlight: Stability and Defect Tolerance. *ACS Energy Lett.* **2017**, *2*, 2071–2083.
- ³⁵ Li, M.; Zhang, X.; Du, Y.; Yang, P. Colloidal CsPbX_3 ($X = \text{Br}, \text{I}, \text{Cl}$) NCs: Morphology Controlling, Composition Evolution, and Photoluminescence Shift. *J. Lumin.* **2017**, *190*, 397–402.

- ³⁶ Tang, X.; Yang, J.; Li, S.; Liu, Z.; Hu, Z.; Hao, J.; Du, J.; Leng, Y.; Qin, H.; Lin, X.; Lin, Y.; Tian, Y.; Zhou, M.; Xiong, Q. Single Halide Perovskite/Semiconductor Core/Shell Quantum Dots with Ultrastability and Nonblinking Properties. *Adv. Sci.* **2019**, *6*, 1900412-1–1900412-10.
- ³⁷ Chouhan, L.; Ito, S.; Thomas, E. M.; Takano, Y.; Ghimire, S.; Miyasaka, H.; Biju, V. Real-Time Blinking Suppression of Perovskite Quantum Dots by Halide Vacancy Filling. *ACS Nano* **2021**, *15*, 2831–2838.
- ³⁸ Efros, A. L.; Nesbitt, D. J. Origin and Control of Blinking in Quantum Dots. *Nat. Nanotechnol.* **2016**, *11*, 661–671.
- ³⁹ Kresse, G.; Furthmüller, J. Efficient Iterative Schemes for Ab Initio Total-Energy Calculations using a Plane-Wave Basis Set. *Phys. Rev. B* **1996**, *54*, 11169–11186.
- ⁴⁰ Miller, G. J. The “Coloring Problem” in Solids: How It Affects Structure, Composition and Properties. *Eur. J. Inorg. Chem.* **1998**, 523–536.
- ⁴¹ White, M. A.; Medina-Gonzalez, A. M.; Vela, J. Soft Chemistry, Coloring and Polytypism in Filled Tetrahedral Semiconductors: Toward Enhanced Thermoelectric and Battery Materials. *Chem. Eur. J.* **2018**, *24*, 3650–3658.
- ⁴² Jepsen, O.; Burkhardt, A.; Andersen, O. K. *The Program TB-LMTO-ASA*, version 4.7; Max-Planck-Institut für Festkörperforschung: Stuttgart, Germany, 1999.
- ⁴³ Roth, A. N.; Chen, Y.; Adamson, M. A. S.; Gi, E.; Wagner, M.; Rossini, A. J.; Vela, J. Alkaline-Earth Chalcogenide Nanocrystals: Solution-Phase Synthesis, Surface Chemistry, and Stability. *ACS Nano* **2022**, *16*, 12024–12035.
- ⁴⁴ Mark, J.; Wang, J.; Wu, K.; Lo, J. G.; Lee, S.; Kovnir, K. Ba₂Si₃P₆: 1D Nonlinear Optical Material with Thermal Barrier Chains. *J. Am. Chem. Soc.* **2019**, *141*, 11976–11983.
- ⁴⁵ Ji, B.; Guderjahn, E.; Wu, K.; Syed, T. H.; Wei, W.; Zhang, B.; Wang, J. Revisiting Thiophosphate Pb₃P₂S₈: A Multifunctional Material Combining a Nonlinear Optical Response and Photocurrent Response. *Phys. Chem. Chem. Phys.* **2021**, *23*, 23696–23702.
- ⁴⁶ Dronskowski, R.; Bloechl, P. E. Crystal Orbital Hamilton Populations (COHP). Energy-Resolved Visualization of Chemical Bonding in Solids Based on Density-Functional Calculations. *J. Phys. Chem.* **1993**, *97*, 8617–8624.
- ⁴⁷ Viezbicke, B. D.; Patel, S.; Davis, B. E.; Birnie, D. P. Evaluation of the Tauc Method for Optical Absorption Edge Determination: ZnO Thin Films as a Model System. *Phys. Status Solidi B* **2015**, *252*, 1700–1710.
- ⁴⁸ Kresse, G.; Hafner, J. Ab initio Molecular-Dynamics Simulation of the Liquid-Metal–Amorphous-Semiconductor Transition in Germanium. *Phys. Rev. B: Condens. Matter Mater. Phys.* **1994**, *49*, 14251–14269.
- ⁴⁹ Blöchl, P. E. Projector Augmented-Wave Method. *Phys. Rev. B: Condens. Matter Mater. Phys.* **1994**, *50*, 17953–17979.
- ⁵⁰ Perdew, J. P.; Burke, K.; Ernzerhof, M. Generalized Gradient Approximation Made Simple. *Phys. Rev. Lett.* **1996**, *77*, 3865–3868.
- ⁵¹ Momma, K.; Izumi, F. J. VESTA 3 for Three-Dimensional Visualization of Crystal, Volumetric and Morphology Data. *J. Appl. Crystallogr.* **2011**, *44*, 1272–1276.

TOC Figure

